

## RESEARCH ARTICLE SUMMARY

## NEURODEVELOPMENT

## Neuron class–specific responses govern adaptive myelin remodeling in the neocortex

Sung Min Yang, Katrin Michel, Vahbiz Jokhi, Elly Nedivi\*, Paola Arlotta\*

**INTRODUCTION:** Myelin is a fundamental structure in the vertebrate nervous system, and its precise formation and regulation are critical for complex neuronal function, including learning and memory. Even small modifications in myelin sheath structure can substantially affect neural network performance. It has been shown that neuronal activity and experience modulate myelination; however, it is unknown whether this plasticity reflects uniform changes across all neuronal subtypes, or whether adaptive myelin remodeling has cell type–specific characteristics that may potentiate circuit tuning, either under normal conditions or driven by experience.

**RATIONALE:** We investigated experience-dependent remodeling of myelination profiles on different

classes of neurons using longitudinal, dual-color in vivo two-photon imaging in the adult neocortex, both during normal vision and through a period of ocular dominance plasticity induced through monocular deprivation (MD). MD is a classical model used to study sensory experience–dependent plasticity, which is known to drive adaptive changes in layer 2/3 (L2/3)  $\gamma$ -aminobutyric acid–releasing (GABAergic) and pyramidal neurons, at both the physiological and the structural level. It has been reported that >90% of the myelin in L2/3 of the neocortex wraps around axons of either excitatory neurons or parvalbumin-expressing GABAergic interneurons (PV-INs). We therefore used MD to interrogate whether sensory experience might drive differential adaptive remodeling

of myelin profiles on excitatory callosal projection neurons (CPNs) versus inhibitory PV-INs.

**RESULTS:** Using genetic identification of cell types, we imaged myelinating oligodendrocytes simultaneously with L2/3 PV-INs or CPNs within the binocular area of primary visual cortex in young adult mice. During normal homeostatic conditions, we found that both excitatory CPNs and inhibitory PV-INs display remodeling of preexisting myelin sheaths as well as de novo generation of myelin segments. Preexisting myelin sheaths present neuronal cell type–specific patterns of plasticity under normal vision, with L2/3 PV-INs displaying a balanced ratio of elongations and contractions, whereas CPNs exhibit shorter myelin sheaths and an overall elongation of segments over time. However, MD elicits an increase in myelin sheath dynamics specifically in PV-INs, whereas CPN myelination remains unchanged from baseline plasticity. This experience-dependent remodeling takes the form of an initial phase of segment elongations followed by a contraction phase that affects a separate cohort of myelin segments. In addition, the adaptive changes in the longitudinal patterns of PV-IN myelination induced by MD are associated with an increase in the displacement rate of putative nodes of Ranvier. Sensory experience does not alter the integration rate of new myelinating oligodendrocytes but can recruit preexisting oligodendrocytes to generate new myelin segments. These changes in PV-INs are accompanied by a concomitant increase in axonal branch tip dynamics during MD that is independent from myelination events.

**CONCLUSION:** Our findings unearth previously unappreciated dynamics of myelin plasticity that are neuron type–specific. We show that even when distinct neuronal subpopulations are interconnected within the same circuit, surrounded by a shared environment, and myelinated by a common set of oligodendrocytes, they display class-specific patterns of myelin changes. The data suggest that adaptive myelination is part of a coordinated suite of circuit reconfiguration processes that are cell type–specific and put forward a conceptual framework in which distinct classes of neocortical neurons individualize adaptive remodeling of their myelination profiles to diversify circuit tuning in response to sensory experience. ■

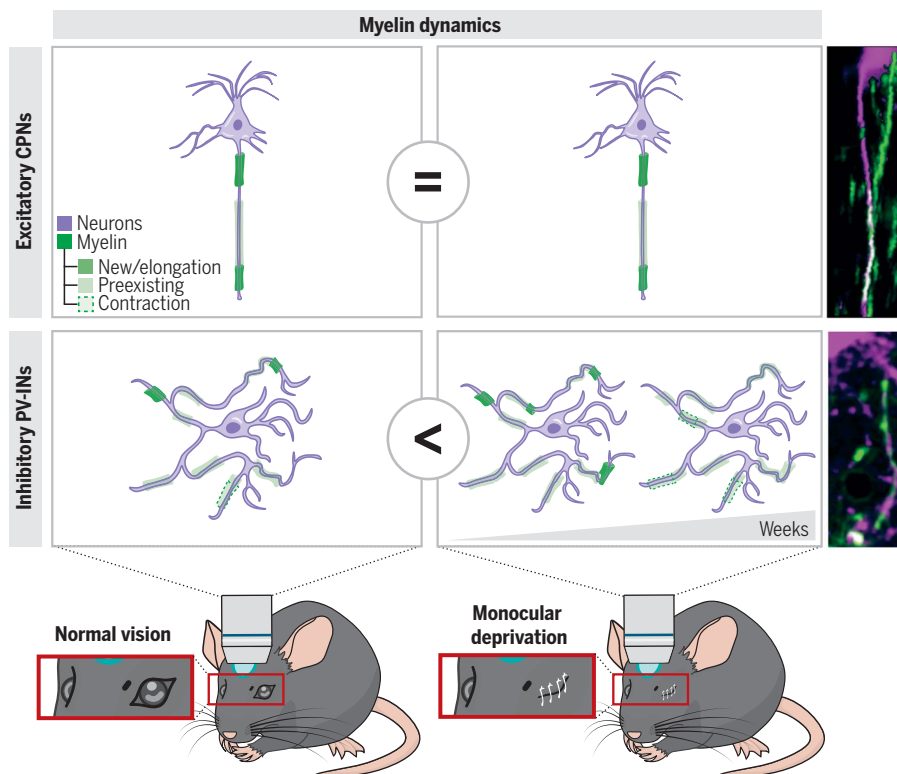
The list of affiliations is available in the full article online.

\*Corresponding author. Email: nedivi@mit.edu (E.N.);

paola\_arlotta@harvard.edu (P.A.)

Cite this article as S. M. Yang et al., *Science* 370, eabd2109 (2020). DOI: 10.1126/science.abd2109

**S** READ THE FULL ARTICLE AT  
<https://doi.org/10.1126/science.abd2109>



**Myelin plasticity is neuron class–specific.** In vivo two-photon imaging is used to show that in normal conditions, L2/3 PV-INs display a balanced remodeling of preexisting myelin sheaths, whereas CPNs present a bias for elongation. MD induces an initial increase in elongating myelin sheaths followed by a phase of contraction in PV-INs, whereas myelin dynamics in CPN remains unaffected by this alteration in sensory experience.

## RESEARCH ARTICLE

## NEURODEVELOPMENT

## Neuron class-specific responses govern adaptive myelin remodeling in the neocortex

Sung Min Yang<sup>1</sup>, Katrin Michel<sup>2</sup>, Vahbiz Jokhi<sup>1</sup>, Elly Nedivi<sup>2,3,4,\*</sup>, Paola Arlotta<sup>1,5\*</sup>

Myelin plasticity is critical for neurological function, including learning and memory. However, it is unknown whether this plasticity reflects uniform changes across all neuronal subtypes, or whether myelin dynamics vary between neuronal classes to enable fine-tuning of adaptive circuit responses. We performed in vivo two-photon imaging of myelin sheaths along single axons of excitatory callosal neurons and inhibitory parvalbumin-expressing interneurons in adult mouse visual cortex. We found that both neuron types show homeostatic myelin remodeling under normal vision. However, monocular deprivation results in adaptive myelin remodeling only in parvalbumin-expressing interneurons. An initial increase in elongation of myelin segments is followed by contraction of a separate cohort of segments. This data indicates that distinct classes of neurons individualize remodeling of their myelination profiles to diversify circuit tuning in response to sensory experience.

**M** yelin is a fundamental cellular structure in the vertebrate nervous system, and its precise formation and regulation are critical for complex neuronal function (1). In vivo imaging studies have shown that myelination in the central nervous system (CNS) continues through adulthood, accompanied by constant remodeling (2, 3). In addition, myelin can be dynamically modulated by neuronal activity and contributes to nervous system plasticity throughout life (4–7). Myelin plasticity in response to experience helps to shape brain structure and function, including learning and memory (6, 8–10). Previous studies of experience-dependent myelin plasticity have demonstrated the importance of myelination by newly formed oligodendrocytes (3–6, 8–11), but the neuronal substrates and dynamic properties of adaptively remodeled myelin segments have not yet been addressed. It has been shown that different neuron subtypes have distinct patterns of axonal myelination, and that myelin profiles vary between individual cells within neuronal classes (12–14); furthermore, callosal and subcortical projection tracts differ in the degree of oligodendrogenesis induced by neuronal activation (4). A major unanswered question, therefore, is whether myelin plasticity affects different neuronal populations homogeneously, or whether adaptive remodeling

has cell type-specific characteristics that may potentiate circuit tuning, either under normal conditions or driven by experience.

## Homeostatic remodeling of preexisting myelin is neuron class-specific

To study experience-dependent remodeling of myelination profiles and oligodendrocyte dynamics in the adult CNS, we used longitudinal dual-color in vivo two-photon imaging in the binocular area of the primary visual cortex (V1b) both during normal vision and through a period of ocular dominance plasticity induced by monocular deprivation (MD) (15). Because >90% of the myelin in layer 2/3 (L2/3) of the neocortex wraps axons of either excitatory neurons [specifically, callosal projection neurons (CPNs)] or parvalbumin-expressing  $\gamma$ -aminobutyric acid–releasing (GABAergic) interneurons (PV-INs) (13), we compared myelin dynamics of these two functionally opposite neuronal classes (Fig. 1, A and B). We used the *Tbr2*<sup>CreERT2</sup>; *CAG*<sup>floaxStop-tdTomato</sup> mouse line to specifically label L2/3 CPNs (fig. S1, A to E) and the *PV*<sup>Cre</sup>; *CAG*<sup>floaxStop-tdTomato</sup> mouse line to label PV-INs (fig. S1, F and G).

We combined this strategy for cell type-specific neuronal labeling with fluorescent detection of myelinating oligodendrocytes using the *P1p1-eGFP* transgenic line, allowing the simultaneous imaging of single axons from each neuronal type (tdTomato<sup>+</sup>), the myelin sheaths wrapping the axons [enhanced green fluorescent protein–positive (eGFP<sup>+</sup>)], and the myelinating oligodendrocytes (Fig. 1, C and D, fig. S2A, and movies S1 and S2). We confirmed that the eGFP signal from *P1p1-eGFP* mice faithfully reflected the presence and length of myelin sheaths, by means of immunohistochemistry against myelin basic protein (MBP) and Cntnpl (also known as Caspr) and by its spatial colocal-

ization with single axonal branches from either CPNs or PV-INs (Fig. 1, E and F, and fig. S2, B to E). We performed long-term in vivo two-photon imaging of layers 1 to 3 V1b in young adult animals [postnatal day 60 (P60) to P90] after the surgical placement of a cranial window and subsequent mapping of V1b using intrinsic optical signal (Fig. 1B).

We first performed two imaging sessions 30 days apart under normal vision to establish baseline changes in myelination. For PV-INs, we traced a total of 292 myelin sheaths [87.6% of which were in L2/3 (Fig. 1G, top)], which were present at a density of  $211 \pm 17$  myelin sheaths per  $10^{-2} \text{ mm}^3$  ( $n = 3$  mice), consistent with the high rate of myelin coverage reported for this type of GABAergic interneuron (13, 14). Contrary to PV-INs, tracing of 47 myelin sheaths on CPNs revealed that most of the CPNs were unmyelinated at P90, with only 20.5% possessing at least a single myelin sheath (fig. S3, A to I). We also found that the onset of CPN myelination occurs late in development (~P30), and the rate of myelination is low but persistent throughout adulthood (4.5% additional myelinated CPNs per month, from P30 to P210) (fig. S3, J to L).

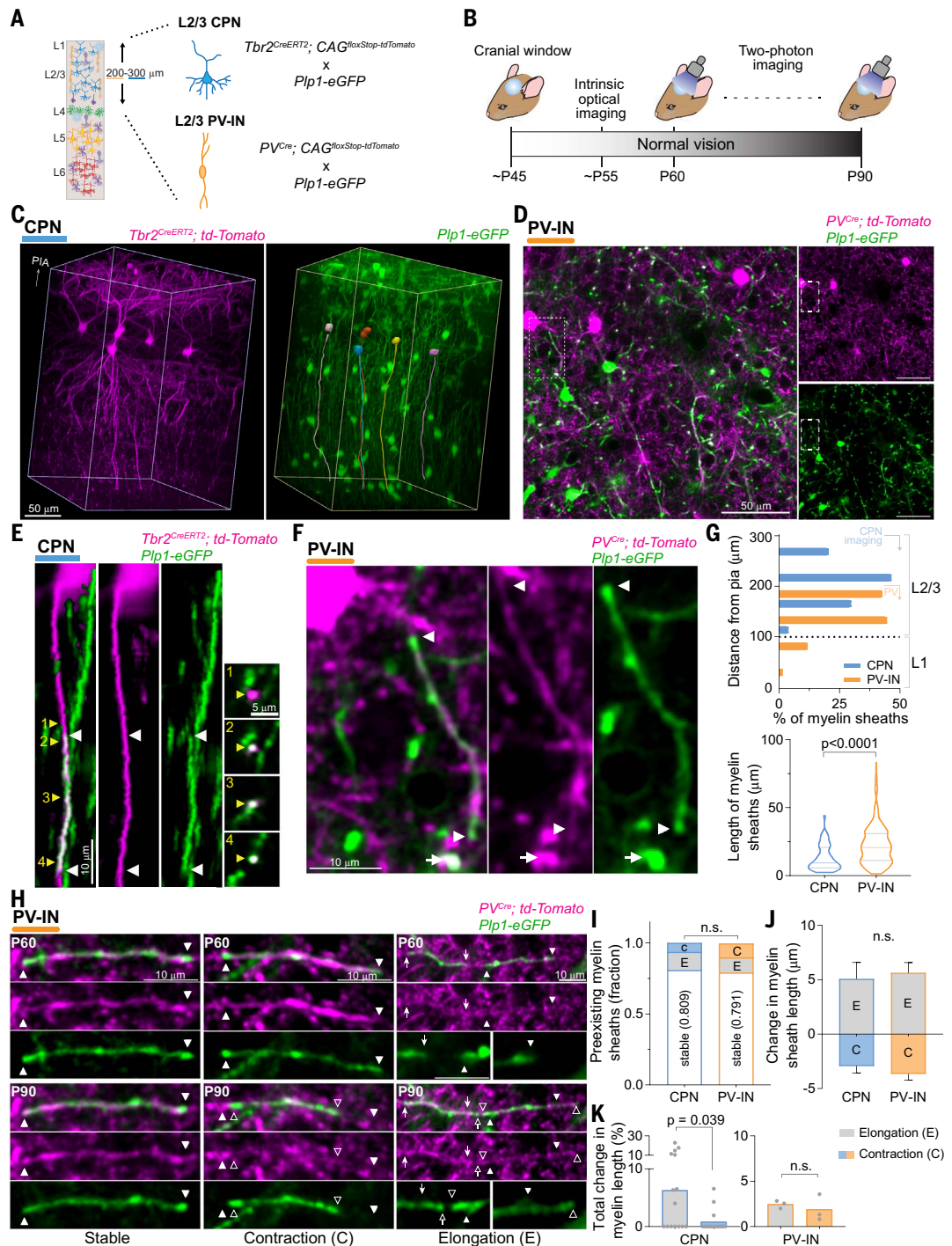
We found that in mice with normal visual experience, the average myelin sheath was longer on PV-INs ( $22.4 \pm 0.7 \mu\text{m}$ ) than on CPNs ( $13.3 \pm 1.3 \mu\text{m}$ ) (Fig. 1G, bottom), which is consistent with previous reports (12, 16). Approximately 20% of the preexisting myelin sheaths on both PV-INs and CPNs changed in length between P60 and P90 (range approximately  $-10$  to  $+20 \mu\text{m}$ ) (Fig. 1, H and I). For PV-INs, the number of elongation (E) and contraction (C) events was similar (E, 10.6% versus C, 10.3%), whereas preexisting sheaths on CPNs showed a greater proportion of elongations (E, 12.7% versus C, 6.4%) (Fig. 1I). Because the average change in sheath length is similar for elongations and contractions (Fig. 1J), the overall remodeling of preexisting myelin sheaths on PV-INs was balanced (E,  $2.5 \pm 0.2\%$  versus C,  $1.9 \pm 0.8\%$ , of total myelin length; Wilcoxon matched-pairs signed rank test,  $P = 0.75$ ,  $n = 3$  mice), whereas there was a net increase in the level of myelination on CPNs (E,  $6.3 \pm 3.5\%$  versus C,  $0.9 \pm 0.5\%$ , of total myelin length; Wilcoxon matched-pairs signed rank test,  $P = 0.039$ ,  $n = 20$  mice) (Fig. 1K). Altogether, these data show that under normal vision, remodeling of preexisting myelin sheaths in the adult neocortex follows neuronal cell type-specific patterns, with L2/3 PV-INs displaying a balanced ratio of elongations and contractions, and CPNs exhibiting shorter myelin sheaths and an overall elongation of segments over time.

## De novo-generated myelin sheaths are more dynamic

The cortex continues to add new myelin sheaths throughout life (2, 3, 10). To test whether

<sup>1</sup>Department of Stem Cell and Regenerative Biology, Harvard University, Cambridge, MA 02138, USA. <sup>2</sup>Picower Institute for Learning and Memory, Massachusetts Institute of Technology, Cambridge, MA 02139, USA. <sup>3</sup>Department of Biology, Massachusetts Institute of Technology, Cambridge, MA 02139, USA. <sup>4</sup>Department of Brain and Cognitive Sciences, Massachusetts Institute of Technology, Cambridge, MA 02139, USA. <sup>5</sup>Stanley Center for Psychiatric Research, Broad Institute of Harvard and MIT, Cambridge, MA 02142, USA. \*Corresponding author. Email: nedivi@mit.edu (E.N.); paola\_arlotta@harvard.edu (P.A.)

### Fig. 1. Preexisting myelin sheaths on L2/3 PV-INs and CPNs present remodeling in young adult mice. (A) Schematic of cell- and myelin-labeling strategy. (B) Experimental time course. Cells in V1b were imaged at P60 and P90. (C) Full imaged volume from a *Tbr2*<sup>Cre</sup> animal in three-dimensional (3D) perspective, showing (left) CPNs imaged simultaneously with (right) oligodendrocytes and myelin. (Right) Skeletal reconstruction of cell bodies and primary axons of tdTomato<sup>+</sup> CPNs are superimposed on the *Plp1-eGFP* image. (D) Representative single frame (~140 μm below pia) showing L2/3 PV-INs along with oligodendrocytes and myelin sheaths. (E and F) Representative images showing myelin sheaths (white arrowheads and arrows) on single axons of a superficial CPN [(E), 3D image, yellow reconstruction in (C)] and a L2/3 PV-IN [(F), single frame, boxed area in (D)]. Yellow arrowheads indicate location of corresponding cross-section insets. (G) Spatial distribution (top) and length (bottom, violin plot) of myelin sheaths at P90. (H) Maximum z projections (MZP) of myelin sheaths on PV-INs, showing stable (left, three frames), contracting (center, three frames), and elongating (right, eight frames) segments. (I) Normalized number of dynamic (elongating and contracting) and stable myelin sheaths. (J) Length change of individual myelin sheaths. (K) Total change in myelin sheath length caused by elongations and contractions of preexisting sheaths. Data are mean ± SEM. Statistics are available in table S1. n.s., not significant.



new myelin segments have distinct dynamic characteristics compared with those of preexisting segments, we performed longitudinal in vivo two-photon imaging on mice with normal visual experience at 1-week intervals between P60 and P90 and analyzed the preexisting (identified in the first imaging session) and de novo (emerging during the course of the 4-week experiment) myelin sheaths on L2/3 PV-INs and CPNs (Fig. 2A). Along with the

longitudinal changes in preexisting myelin sheaths described in the previous section, we found a high number of new myelin sheaths (~19.7% of total segments at P90) (Fig. 2, B and C) on both CPNs and PV-INs. De novo-generated myelin sheaths had similar lengths as those of preexisting sheaths, so that the myelin length distributions across new and preexisting segments were indistinguishable, for both neuronal populations (Fig. 2D). In PV-

INs, new myelin segments were continuously produced, with new segments identified in 15 out of the 16 weekly imaging sessions (Fig. 2, E and F) (the number of new segments in CPNs was not large enough to enable detailed analysis). The integration of new myelinating oligodendrocytes was rare (three new oligodendrocytes across four mice), but in imaging sessions with new myelinating oligodendrocytes, we saw an almost fivefold increase in both the

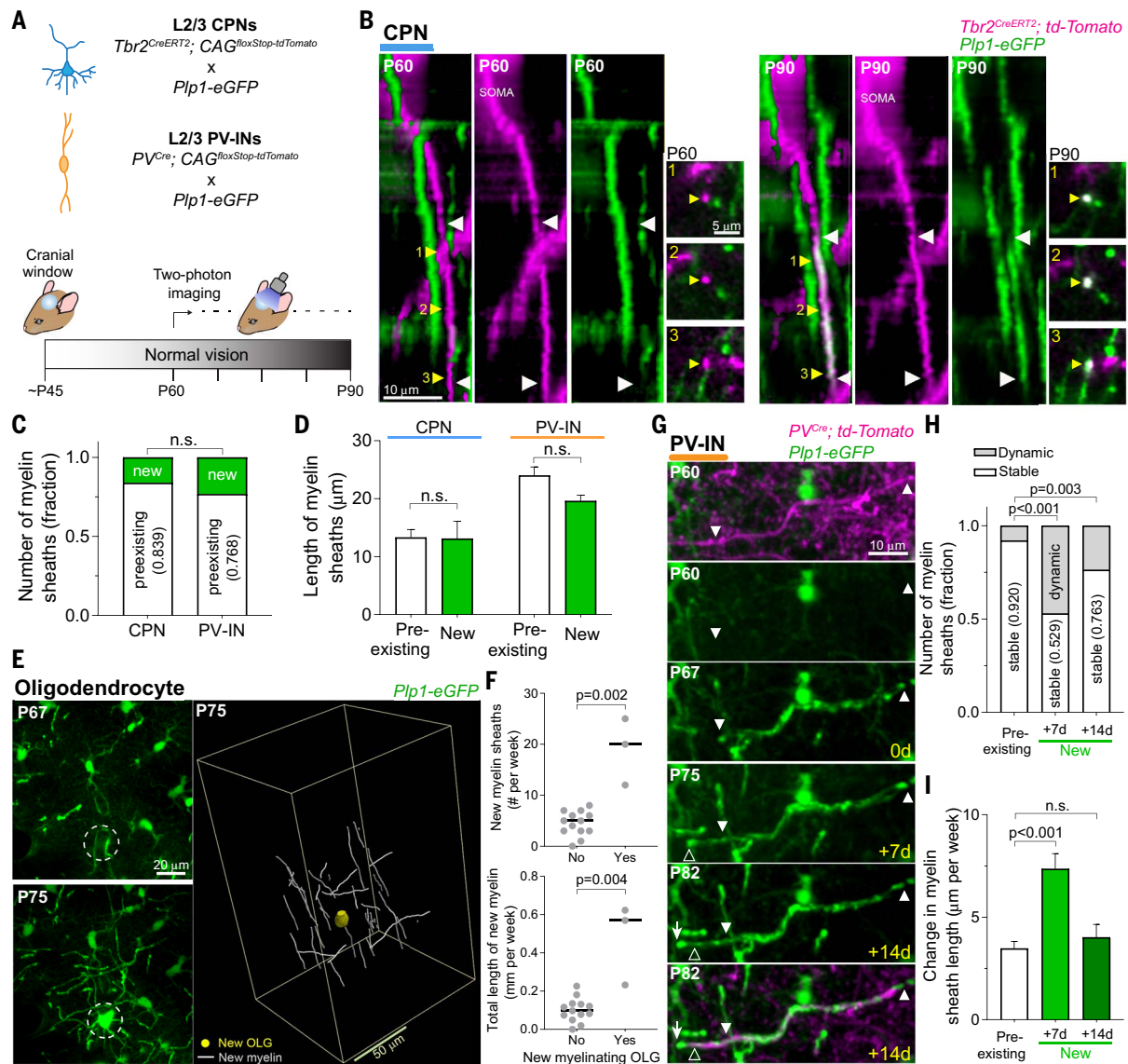


**Fig. 2. De novo-generated myelin sheaths are more plastic than preexisting sheaths in PV-INs.** (A) Schematic of cell- and myelin-labeling strategy (top) and experimental time course (bottom). Cells were imaged weekly between ~P60 and ~P90. (B) Representative 3D images displaying a new myelin sheath (white arrowheads) generated on a single CPN axon. Yellow arrowheads indicate the location of corresponding cross-section insets. (C) Fraction of preexisting and de novo-generated myelin sheaths at P90, using P60 as baseline. (D) Length of individual myelin sheaths at P90. (E) MZP (15 frames) showing the integration of a new myelinating oligodendrocyte (left, circle) and 3D reconstruction of newly generated myelin sheaths on PV-INs, surrounding the cell body of the new

oligodendrocyte (OLG; right). (F) Number (top) and total length (bottom) of new myelin sheaths on PV-INs, when a new myelinating oligodendrocyte was present (Yes) or not (No) within the imaged volume. Each dot indicates a single imaging session. (G) MZP (14 frames) displaying the remodeling of a de novo-generated myelin segment on a PV-IN. Timeline in yellow is relative to the first session in which we detected the new sheath. (H and I) Normalized number of dynamic and stable myelin sheaths (H), and change in sheath length (I). Data represents new segments on PV-INs at time points 1 and 2 weeks after the session in which they were first identified [see (G)], compared with the preexisting sheaths. Data are mean  $\pm$  SEM. Statistics are available in table S1. n.s., not significant.

rate of de novo generation of myelin segments and the total length of added myelin (Fig. 2F).

We next examined the level of remodeling of new sheaths analyzing with preexisting sheaths, by analyzing the imaging session in which individual new sheaths were first identified and sessions 1 and 2 weeks later (Fig. 2G). Newly formed oligodendrocytes generate all of their myelin segments within 3 days of their differentiation (17, 18), which is well within

these imaging intervals. Although both new and preexisting sheaths showed elongation and contraction, the new myelin segments exhibited a much larger ratio of elongations to contractions (54 E: 3 C, new sheaths; 31 E: 30 C, preexisting sheaths). Of the new myelin sheaths, 47.1% displayed changes in length during the first week after they were first detected, whereas only 8.0% of preexisting sheaths were remodeling during the same period (Fig. 2H).

The change in length of individual sheaths was also two times larger for new sheaths compared with preexisting myelin (Fig. 2I). Moreover, the remodeling rate of new sheaths remained higher than that of preexisting sheaths for at least 2 weeks after their generation.

Thus, although rarer, new myelin sheaths are more dynamic than preexisting myelin in PV-INs and greatly contribute to myelin plasticity in young adult mice.

### Experience-dependent myelin remodeling is neuron type-specific

It is unclear whether experience-dependent reconfiguration of neuronal circuits is accompanied by a remodeling of myelination profiles in a homogeneous or a cell type-specific fashion. Therefore, we compared the changes in myelin dynamics and the integration rate of new myelinating oligodendrocytes before and during monocular deprivation. MD is a model of sensory deprivation that induces a shift in response properties in both L2/3 inhibitory interneurons and pyramidal neurons in V1b (15, 19), accompanied by remodeling of dendritic and axonal compartments (20, 21). How MD affects myelin plasticity has not been established.

We performed eyelid suture immediately after 14 days of weekly imaging under normal vision (three sessions, 1 week apart), followed

by 2 weeks of imaging under MD (imaging at 4, 7, and 14 days of MD), and studied the longitudinal distribution of myelin segments along single axons in V1b (Fig. 3A). We imaged 39 mice for L2/3 CPNs (Fig. 3B) and nine mice for L2/3 PV-INs (Fig. 3F). For each animal, we examined the number of dynamic events and their length changes, for both preexisting and new myelin segments.

First, we compared the weekly rate of sheath dynamics on CPNs during the 2 weeks of normal vision and the subsequent 2 weeks of MD (Fig. 3, C and D) and found that the rate of remodeling remained unchanged (before,  $10.0 \pm 1.8\%$  per week versus MD,  $10.3 \pm 2.4\%$  per week; paired *t* test,  $P = 0.933$ ;  $n = 39$  mice, 146 sheaths). Similarly, MD did not affect the cumulative change in myelin length caused by the population of dynamic sheaths (percent of total length per week: before,  $5.6 \pm$

1.4% versus MD,  $4.6 \pm 1.8\%$ ; paired *t* test,  $P = 0.647$ ) (Fig. 3E). We measured the rate of dynamic sheaths and the normalized cumulative change in myelin length for each category of remodeling (elongation, contraction, and de novo generation) and determined that MD did not alter either of these parameters for any of the remodeling categories (fig. S4). These results indicate that MD does not affect the plasticity of myelination profiles in L2/3 CPNs.

Next, we asked whether L2/3 PV-INs had myelin dynamics in response to MD similar to that of their CPN neighbors (Fig. 3G). In contrast to CPNs, we observed an increase in the rate of dynamic myelin sheaths (before,  $11.9 \pm 1.3\%$  per week versus MD,  $20.3 \pm 1.5\%$  per week; paired *t* test,  $P = 0.0006$ ;  $n = 9$  mice, 2465 sheaths) (Fig. 3H), and in seven out of nine mice, there was also an increase in the

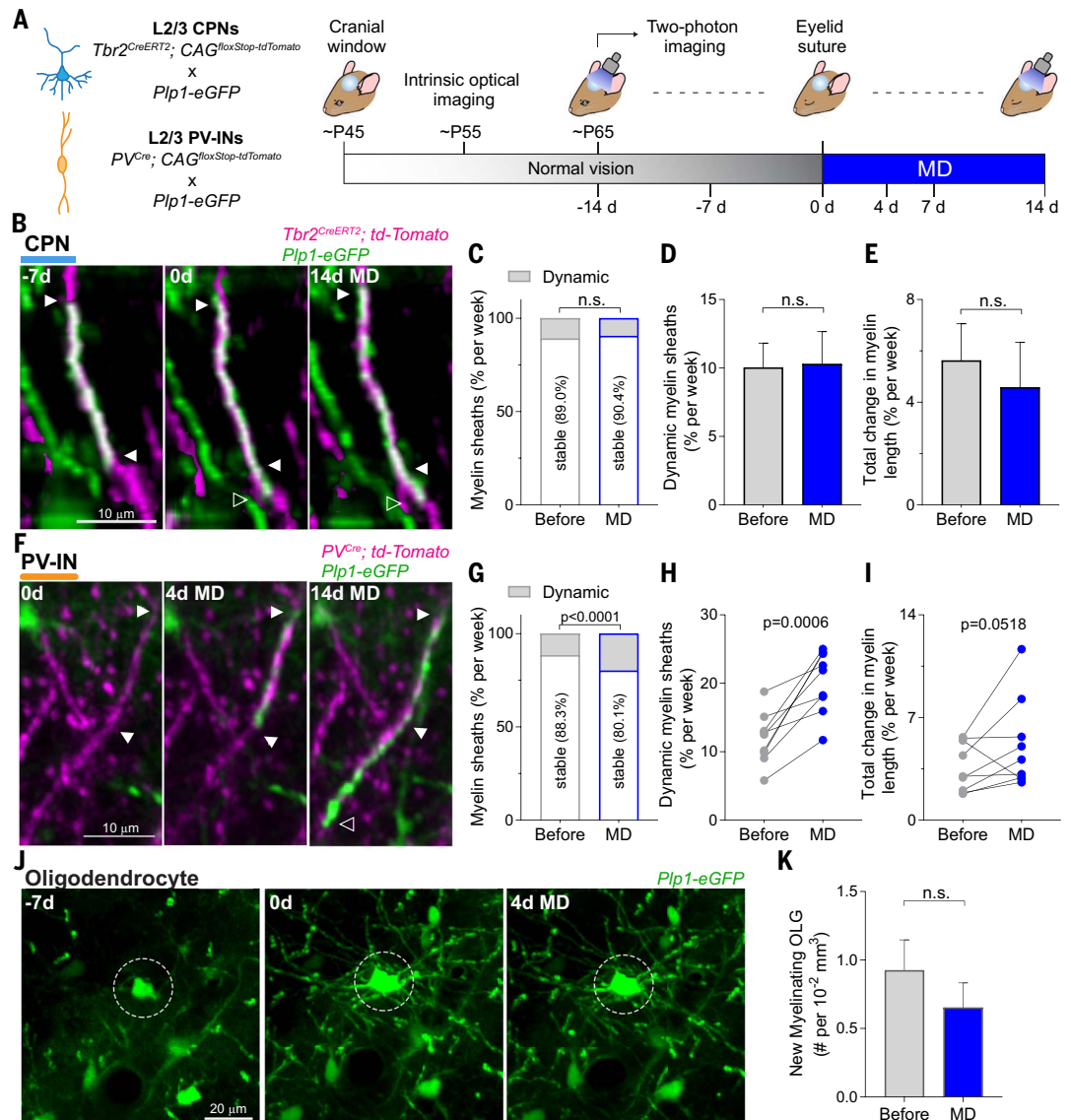
### Fig. 3. Experience-dependent remodeling of myelination profiles is neuron class-specific.

(A) Schematic of cell- and myelin-labeling strategy (left) and experimental time course (right). Cells in V1b were imaged at each indicated time point. (B) Representative 3D images of an elongating CPN myelin sheath.

(C) Fraction of stable and dynamic myelin sheaths on CPNs (combined data from all mice). The data represent the average of two 1-week intervals between time points, during the periods before (–14 versus –7 days and –7 versus 0 days) and during MD (0 versus 7 days and 7 versus 14 days). (D) Rate of myelin sheath dynamics for CPNs. Each mouse was analyzed as an independent statistical replicate ( $n = 39$  mice). (E) Rate of change in sheath length elicited by myelin remodeling.

(F) MZP (five frames) of a newly generated myelin sheath on a PV-IN. (G to I) Analysis of PV-IN myelination ( $n = 9$  mice), corresponding to (C) to (E). (J) MZP (22 frames) of a new myelinating oligodendrocyte (circle, 0 days). The circled cell at –7 days is likely an oligodendrocyte progenitor cell.

(K) Number of new myelinating oligodendrocytes integrated in the 2-week intervals before and during MD ( $n = 19$  mice). Data are mean  $\pm$  SEM. Statistics are available in table S1. n.s., not significant.



cumulative change in their length (Fig. 3I). This increase in myelin sheath dynamics in PV-INs is exclusive to the binocular visual cortex and is absent in monocular visual cortex (fig. S5), indicating that the changes are associated with the ocular dominance shift induced by MD (fig. S6). These findings demonstrate that sensory experience drives adaptive remodeling of myelination profiles specifically in PV-INs, whereas CPN myelination shows only a continuation of baseline plasticity.

Last, because new oligodendrocytes account for a substantial fraction of myelin remodeling under normal vision (Fig. 2), we investigated the integration rate of new myelinating oligodendrocytes during MD (Fig. 3J). The initial density of mature oligodendrocytes was  $47.1 \pm 1.6$  cells per  $10^{-2}$  mm<sup>3</sup> (P65,  $n = 19$  mice), and the integration rate of new myelinating oligodendrocytes did not change upon MD (new myelinating oligodendrocytes per  $10^{-2}$  mm<sup>3</sup>; before,  $0.92 \pm 0.22$  versus MD,  $0.65 \pm 0.18$ ; Wilcoxon matched-pairs signed rank test,  $P = 0.542$ ,  $n = 19$  animals) (Fig. 3K), in either L1 or L2/3 (fig. S7, A to D). Furthermore, we found no changes in the proliferation or apoptosis of oligodendrocyte precursor cells upon MD (fig. S7, E to I), nor any elimination of mature oligodendrocytes. These data reveal an unprecedented level of specificity for myelin plasticity, demonstrating that MD-induced adaptive remodeling of myelination profiles is neuron class-specific and is sufficient to achieve circuit reconfiguration without the need for integration of new myelinating oligodendrocytes.

### Temporal dynamics of adaptive myelin remodeling in PV-INs

GABAergic neurons in L2/3 of adult mouse V1b respond to MD with changes in their dendritic arbors that first undergo retraction and subsequently elongate (20). Therefore, we asked whether the experience-dependent increase in myelin dynamics in PV-INs also follows a defined spatiotemporal pattern (Fig. 4A). We analyzed myelin dynamics over the time course of MD and found that PV-INs presented a two-phase sequence of myelin dynamics. Throughout the first week of MD, there was an acute increase in myelination, through more frequent elongation of preexisting sheaths (threefold increase in rate) and the generation of new myelin segments (Fig. 4, B and C, and fig. S8, A to D). In the second week (7 to 14 days MD), the elongation rate returned to baseline levels, accompanied by threefold increases in contractions and in the cumulative change in length (Fig. 4, B and C). We also observed full elimination of myelin segments upon MD in PV-INs (fig. S9, A and B). This extreme form of contraction was not seen in PV-INs during normal visual experience or in CPNs. MD also caused the recruitment of preexisting oligo-

dendrocytes to produce new myelin segments on PV-INs (Fig. 4D, fig. S9C, and movie S3). These results show that MD triggers a series of events that progressively modify the myelination profile of PV-INs.

We next asked whether the myelin remodeling induced by MD represented an acceleration of baseline remodeling or had different dynamics. Under normal vision, consecutive changes of a single myelin sheath length were always in the same direction—either successive elongations or successive contractions (Fig.

4E). By contrast, during MD,  $25.5 \pm 1.4\%$  of successive changes on a single segment were in opposite directions (Fig. 4E), indicating that MD altered the pattern of myelin remodeling. We next asked whether the myelin sheaths remodeled during MD were the same as those affected during normal vision. From the entire population of dynamic sheaths, 56.7% presented changes exclusively during MD, whereas 22.2% were dynamic solely under normal vision (Fig. 4F), indicating that MD triggers the remodeling of a different set of sheaths rather than

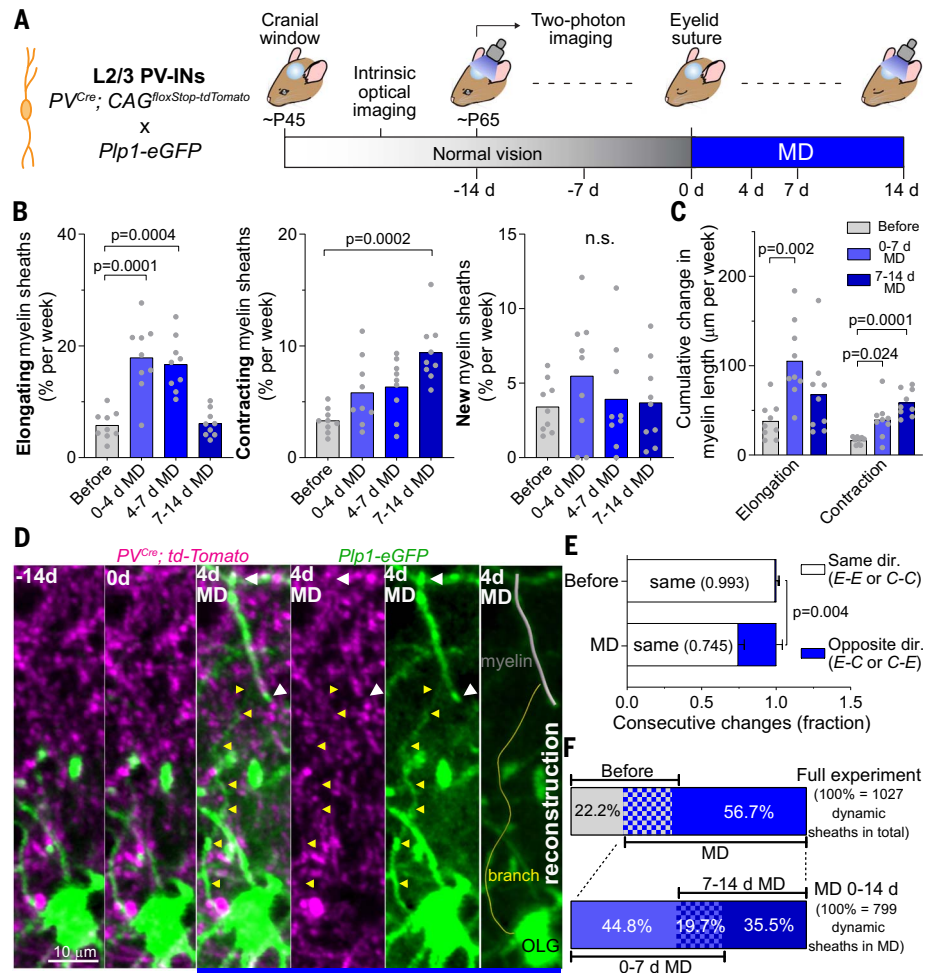


**Fig. 4. MD elicits temporally distinct phases of myelin dynamics in PV-INs.** (A) Schematic of PV-IN and myelin labeling strategy (left) and experimental time course (right). (B) Rate of myelin sheath elongation (left), contraction (center), and de novo generation (right) in PV-INs before and during MD. Each dot indicates an animal. The data before MD (−14 to 0 days) was combined into a single group (before). (C) Rate of absolute cumulative change in sheath length produced by contractions and elongations. (D) MZP (five frames) showing a preexisting oligodendrocyte (OLG) generating a new myelin sheath (white arrowheads) on a PV-IN during MD. Yellow arrowheads indicate the branch that connects the myelin segment to the OLG cell body. A 3D reconstruction is displayed at far right. (E) Fraction of changes in individual sheaths over consecutive imaging sessions classified by the different combinations of change direction: same (elongation-elongation or contraction-contraction) and opposite (elongation-contraction or contraction-elongation). (F) (Top) Percentage of myelin sheaths presenting changes only before MD (gray), only during MD (blue), and in both conditions (gridded, 21.1%). (Bottom) Percentage of myelin sheaths presenting changes only during the first week of MD (lighter blue), only the second week of MD (darker blue), and during both weeks of MD (gridded). Data are mean  $\pm$  SEM. Statistics are available in table S1. n.s., not significant.

continuing changes in previously dynamic sheaths. Moreover, a total of 80.3% of sheaths that were dynamic during MD exhibited changes only during the elongation phase (0 to 7 days MD, 44.8%) or the retraction phase (7 to 14 days MD, 35.5%), but not both, indicating that the opposite phases affect two different subgroups of myelin segments (Fig. 4F). In particular,  $54.0 \pm 0.9\%$  of contracting sheaths during the second week of MD had shown no change until then (versus  $26 \pm 5\%$  of elongating sheaths) (fig. S8E).

These results indicate that MD drives the remodeling of myelin profiles in L2/3 PV-INs by recruiting previously stable myelin segments in two separate phases: first triggering a wave of elongation events, followed by contraction of a different group of myelin sheaths. These previously unknown myelin dynamics distinguish the response to sensory perturbation from baseline myelin plasticity.

### MD induces remodeling on PV-IN axons

Because myelin placement relates to the structure and function of axons (1, 22), we interrogated the relationship between myelin plasticity and changes in axonal morphology and structure (Fig. 5A). We investigated the impact of sensory experience on the nodes of Ranvier, short unmyelinated segments that are occupied by clusters of ion channels (fig. S2F). It has been shown that changes in myelin structure are accompanied by changes in length of these nodes, which modify action potential propagation along the axon (23). We examined the dynamics of putative nodes of Ranvier in PV-INs (Fig. 5B), which are defined as short nodes ( $<5 \mu\text{m}$ ) separating two neighboring myelin sheaths. We found that putative nodes of Ranvier can be displaced along the axon during MD (14 out of 257 nodes in nine mice; distance,  $2.66 \pm 0.25 \mu\text{m}$ ) as a result of the contraction of one sheath and the elongation of another (Fig. 5C). By contrast, node displacement was rarely seen under normal vision (3 out of 257 nodes). This result suggests that MD induces changes in the longitudinal patterns of PV-IN myelination and an associated increase in the rate of displacement of putative nodes of Ranvier.

Visual manipulations have been shown to induce reorganization of inhibitory neuron axons in adult visual cortex (24). We therefore examined axonal arbor remodeling in PV-INs, focusing on those branches that were myelinated (Fig. 5D and fig. S10A). We found that myelin remodeling overwhelmingly occurred on axonal branches that did not exhibit changes in length during MD ( $95.4 \pm 0.7\%$  of axons showing myelin remodeling) (fig. S10B). This indicates that the experience-dependent remodeling of myelination profiles in PV-INs is not simply a downstream effect of axonal remodeling.

MD also resulted in an increased number of dynamic axonal branch tips in PV-INs (Fig. 5E) as well as a greater cumulative change to axonal length (fig. S10C). In agreement with our findings that MD did not affect CPN myelin plasticity, we did not observe axon remodeling in these neurons (0 out of 68 neurons). Our results indicate that PV-INs show independent increases in both axonal branch remodeling and myelin plasticity in response to MD.

Altogether, the data point toward adaptive myelination as part of a coordinated circuit-reconfiguration process, which acts through differential responses by individual neuronal subtypes to perturbations in sensory experience.

### Discussion

Prior reports have shown that neuronal activity and experience modulate myelination (4, 7, 11, 17, 25, 26) and that active myelination by newly formed oligodendrocytes is necessary for learning and memory (8–10). Understanding the dynamic mechanisms that govern myelin plasticity and how they relate to other mechanisms of neuronal plasticity remains a fundamental question.

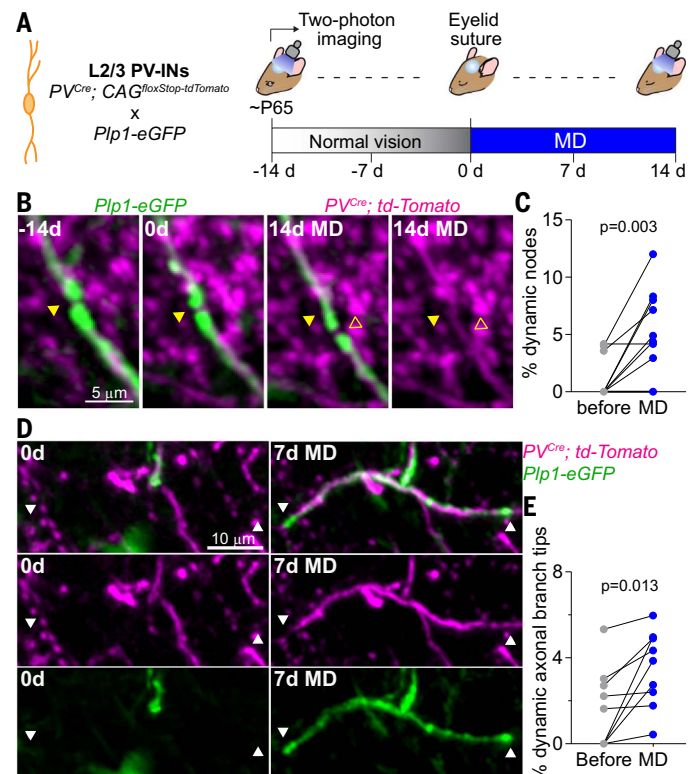
We found that sensory deprivation (MD) induces adaptive myelin remodeling in a neuron class-specific manner, highlighting unexpected levels of specificity in neuron-oligodendrocyte interaction. The response to MD is complex,

unfolding in an age-dependent and time-specific manner across multiple neuron types (27–29). However, it has been shown that L2/3 interneurons show greater electrophysiological and structural plasticity in response to MD compared with pyramidal cells (19–21, 29). In particular, after MD there is an initial phase of dendritic branch tip retractions in L2/3 inhibitory neurons, followed by a second phase of balanced growth and retraction (20). We found that L2/3 PV-INs likewise show a biphasic increase in myelin plasticity upon MD compared with CPNs. During the first week after MD, there is an increase in PV-IN myelination, whereas in the second week, there is a concerted increase in myelin sheath retraction. However, MD-induced myelin remodeling was primarily restricted to axonal branches that did not change in length, suggesting that myelin plasticity is part of an orchestrated set of circuit reconfiguration processes rather than simply a consequence of axonal remodeling. It would be informative to use electron microscopy to further investigate whether other structural changes, such as myelin thickness and axon caliber, are taking place along with the remodeling of myelination profiles.

Our results demonstrate that MD does not stimulate the integration of new myelinating oligodendrocytes. Rather, it induces remodeling of preexisting myelin sheaths on PV-INs,

**Fig. 5. Sensory experience drives changes in the axonal arbor of PV-INs.** (A) Schematic of fluorescence labeling strategy and experimental time course.

(B) Single-frame images showing a putative node of Ranvier (arrowheads) between two neighboring myelin sheaths, and a shift of its location during MD. (C) Number of relocated putative nodes of Ranvier in the 2-week intervals before and during MD. (D) MZP (six frames) showing a new myelin sheath generated on a new axonal branch. (E) Number of dynamic axonal branch tips in the 2-week intervals before and during MD. Each dot indicates an animal [(C) and (E)]. Statistics are available in table S1.



including contraction and full elimination of myelin sheaths. Small modifications in myelin sheath structure can be sufficient to substantially affect neural network function (30). We speculate that the reconfiguration of network connectivity that underlies a functional ocular dominance shift likely requires a fine and precise tuning of individual myelination profiles instead of a broad addition of myelin (22, 30, 31). In line with this hypothesis, we observed recruitment of preexisting oligodendrocytes to generate new myelin sheaths. This finding is in agreement with recent reports that surviving oligodendrocytes can establish new myelin segments in a cuprizone-induced model of oligodendrocyte death and demyelination (17). Our data now indicates that in response to sensory manipulation, new myelin segments are produced by both newly formed and preexisting oligodendrocytes.

The data demonstrate cell type-specific dynamics of myelin plasticity, even when the distinct neuronal subpopulations are interconnected within the same circuit, surrounded by a shared environment, and myelinated by a common set of oligodendrocytes. These findings suggest a framework for conceptualizing experience-dependent myelin plasticity, in which cell type-specific adaptive remodeling of myelination allows different neurons to modify their individual functions and potentiates the tuning capacity of neuronal networks.

## Materials and methods

### Mice

We used the following genetically modified mouse lines: Plp1-eGFP (32), Pvalb<sup>tm1(cre)Arbr</sup> (PV<sup>Cre</sup>; RRID: IMSR\_JAX\_017320) (33), Tbr2<sup>CreERT2</sup> (34) and B6;129S6-Gt(ROSA)26Sor<sup>tm14(CAG-tdTomato)Hze/J</sup> (CAG<sup>floxStop-tdTomato</sup>; RRID: IMSR\_JAX\_007909; Ai14) conditional reporter line (35). Mice from these lines were crossed to generate PV<sup>Cre/+</sup>; tdTomato<sup>+/-</sup>; Plp1-eGFP<sup>+/-</sup> mice and Tbr2<sup>CreERT2/+</sup>; tdTomato<sup>+/-</sup>; Plp1-eGFP<sup>+/-</sup> mice to label oligodendrocytes along with parvalbumin-expressing interneurons (PV-INs) and callosal projection neurons (CPNs), respectively. This fluorescence labeling strategy allowed us to visualize myelinating oligodendrocytes and myelin sheaths by eGFP, simultaneously with neuronal cell bodies and axons by tdTomato. To generate the well-isolated labeling required for in vivo imaging, we optimized the tamoxifen induction protocol for the Tbr2<sup>CreERT2</sup>; CAG<sup>floxStop-tdTomato</sup> mouse line to sparsely label only the CPNs in the most superficial portion of L2/3 (Fig. 1C and fig. S1, D and E). Then, to induce tdTomato expression in the Tbr2<sup>CreERT2</sup> line, pregnant mice were injected at embryonic day 18.5 (E18.5) with 4-hydroxytamoxifen (Sigma-Aldrich, CAS Number: 68392-35-8) in corn oil (single dose of 1 mg tamoxifen per kg body weight); this induction protocol was used for all subsequent experiments.

Mice were maintained on a C57BL/6J background, and both male and female mice were used for experiments. All procedures were designed to minimize animal suffering and approved by the Harvard University Institutional Animal Care and Use Committee, and the Massachusetts Institute of Technology Committee on Animal Care, and performed in accordance with institutional and federal guidelines.

### Surgical procedure

To allow long-term visualization of in vivo neuronal morphology and myelination profiles, a 5 mm glass coverslip replacing a skull area (cranial window) was implanted over the right visual cortex of young adult mice (P42–P49) as previously described (36). Two to three weeks later, optically clear windows were selected for in vivo two-photon imaging. Animals were housed in groups of 2 to 4 mice per cage from weaning until 1 week before the first session of imaging (P60–P71); then, mice were singly housed for the remainder of the experiment. Sulfamethoxazole (1 mg ml<sup>-1</sup>) and trimethoprim (0.2 mg ml<sup>-1</sup>) were chronically administered in the drinking water through the final imaging session to maintain optical clarity of implanted windows.

### Optical intrinsic signal imaging

For functional identification of monocular and binocular visual cortex (V1b), optical imaging of intrinsic signal and data analysis were performed as described previously (20). Briefly, animals were mildly anesthetized with 0.75 to 1% isoflurane, restrained using a head mount, and placed facing a monitor. For visual stimuli, a horizontal bar (5° in height and 73° in width) drifting up with a period of 12 s was presented for 60 cycles on a high-refresh-rate screen positioned 25 cm in front of the animal. Images were acquired continuously under 610-nm illumination with an intrinsic imaging system (LongDaq Imager, Optical Imaging) through a 2.5X/0.075 NA objective (Zeiss). Cortical intrinsic signal was computed by extracting the Fourier component of light reflectance changes matched to stimulus frequency from 4 by 4 spatially binned images. The fractional change in reflectance represents response magnitude, and the magnitude maps were thresholded at 30% of the peak-response amplitude to define a response region. Primary visual cortex was determined by stimulation of both eyes, while V1b was determined by stimulation of the ipsilateral eye. Monocular visual cortex was determined by subtracting the V1b map from the map of primary visual cortex.

### Two-photon imaging

After identifying the binocular visual cortex through optical intrinsic signal imaging and allowing sufficient time (about 3 weeks) for recovery from the cranial window surgery,

young adult mice were anesthetized (1 to 1.25% isoflurane) and head fixed in a stereotaxic frame for large-volume, high-resolution dual-color imaging using a custom-built two-photon microscope. Since tdTomato and eGFP were used to label neurons and oligodendrocytes, respectively, the two fluorophores were simultaneously excited with a Mai Tai HP Ti:Sapphire laser (Spectra-Physics) set at 975 nm (CPN experiments) or 990 nm (PV-IN experiments) and pumped by a 14 W solid state laser delivering 100 fs pulses at a rate of 80 MHz. A 200 by 200 by 300 μm (CPN) or 200 by 200 by 200 μm (PV-IN) neuronal volume at 250 nm/pixel XY was acquired for each mouse by scanning the laser beams using galvanometric XY-scanning mirrors (6215H, Cambridge Technology). 0.8 μm/frame Z-resolution was achieved using a piezo actuator positioning system (Piezosystem, Jena). The output power from the 20X/1.0 NA water immersion objective (W Plan-Apochromat, Zeiss) was set to 50 mW. The emission signals were collected using the same objective, passed through an IR blocking filter (E700SP, Chroma Technology), and spectrally separated using a dichroic mirror at 560 nm. Emission signals were simultaneously collected with two independent photomultiplier tubes after passing through the appropriate bandpass filters (550/100 and 605/75). Then, two-photon raw data were processed for spectral linear unmixing as described previously (37) and the images were converted to an RGB image z-stack using a home-built MATLAB script.

### Monocular deprivation

Monocular deprivation was performed by eyelid suture immediately after the third imaging session (2 weeks of imaging under normal vision). Mice were anesthetized with 2% isoflurane, lid margins were trimmed, and triple antibiotic ophthalmic ointment (Bausch & Lomb) was applied to the eye. Four to five individual sutures were placed using 6-0 vicryl along the extent of the trimmed lids. Suture integrity was inspected directly before each imaging session. Animals whose eyelids did not seal fully or had reopened were excluded from further experiments.

### Measurement of ocular dominance

Ocular dominance during normal condition and after monocular deprivation was determined from optical intrinsic signal images as previously described (38). The ocular dominance index (ODI) was calculated from the average of  $(C - I)/(C + I)$  for all pixels in the region identified as binocular visual cortex, where  $C$  and  $I$  represent the response magnitude of each pixel to the contralateral and ipsilateral eyes, respectively. The ODI ranges from +1 to -1, where a positive value indicates a contralateral bias and a negative value an ipsilateral bias.

### Analysis of fluorescence images

In vivo  $z$ -stacks collected from  $PV^{Cre/+}; td\text{-Tomato}^{+/-}$ ;  $Plp1\text{-eGFP}^{+/-}$  (to investigate myelination on PV-IN) and  $Tbr2^{CreERT2/+}; td\text{-Tomato}^{+/-}$ ;  $Plp1\text{-eGFP}^{+/-}$  (to study myelination on CPN) mice were acquired using two-photon microscopy. Data analysis was performed blind to the experimental conditions. Images were randomized (consecutive time points were paired for further comparisons) for analysis by blinded observers. To eliminate any hint about the experimental condition, the last imaging session was paired with the first one; the results from the latter comparison was used to validate the intermediate changes between consecutive sessions.

### Identifying myelin sheaths along single axons

Image  $z$ -stacks and time-series were traced and analyzed using NeuroLucida (MicroBrightField) and FIJI/ImageJ (NIH). All analysis was performed on unprocessed images, and for presentation in figures, image brightness and contrast levels were adjusted for clarity. For CPN experiments, cell bodies and their primary axons were segmented using the voxel scooping method for a semi-automated tracing in NeuroLucida (axonal arborization of PV-INs were not segmented because of their extreme complexity and density). Then, the eGFP<sup>+</sup> processes colocalizing to tdTomato<sup>+</sup> axonal processes were also segmented, in both CPN and PV-IN experiments. eGFP<sup>+</sup> processes were scored as myelin sheaths if they presented colocalization of at least 80% extension to a tdTomato<sup>+</sup> axon, the centerlines of the eGFP<sup>+</sup> process and tdTomato<sup>+</sup> axon underneath were separated no further away than 2 pixels (0.5  $\mu\text{m}$ ), and the structures have a minimal average signal intensity of at least four times above shot noise background levels. Myelin paranodes were identified by increased eGFP fluorescence intensity (Fig. 1). A gap in the fluorescence signal greater than 1.6  $\mu\text{m}$  was used to designate a break in the myelination and classified as a different myelin sheath. Myelin sheaths with terminals that could be confidently identified across all imaging sessions, not extending beyond the imaging volume or obscured by blood vessels, were monitored and included to further analysis.

The depth of each myelin sheath was determined by its midpoint along the axial position, relative to the pial surface, and verified by the L1-L2/3 border at approximately 90  $\mu\text{m}$  below the pia. The interphase between L1 and L2/3 was identified in the  $z$ -stacks by the high density of cell bodies in L2/3 and also through post hoc DAPI staining. L2/3 CPNs have axonal projections extending subcortically through the deeper layers of the cortex as well as long projections to the contralateral hemisphere. Since the myelin analysis was restricted to L1-L3 of the ipsilateral cortex, the proportion of

myelinated CPNs we have reported is likely an underestimation.

### Analyzing myelin sheath dynamics

Changes in myelin sheath length were independently validated by two investigators, using the intersection of cellular processes as stable landmarks across images to set reference lines (changes in xy plane) or identify equivalent frames (changes in  $z$  direction). Double confirmation by two investigators was required for a change in length to be included for further analysis. For changes in myelin length with a perpendicular orientation to images stacks, we set an inferior threshold of 1.6  $\mu\text{m}$ , while for changes with a lateral orientation the threshold was set at 1.25  $\mu\text{m}$ . In addition, we discarded the changes in length <2.0  $\mu\text{m}$  that were followed by partial or complete reversion in the change, assuming them to be false-positive cases generated by the intrinsic variability across imaging sessions over a stable sheath.

For each mouse, the percentage of myelin sheaths elongating or retracting between two successive imaging sessions, relative to the total sheath number of the previous imaging session, were defined as the rates of myelin sheath elongations and contractions, respectively. Contractions included both retractions of existing sheaths as well as the elimination of entire segments (we observed only 12 cases of full elimination in total), while elongations and generation of new myelin sheaths were analyzed separately. Rate of sheath dynamics was defined as the sum of the rates of sheath elongations, contractions and de novo generations. For all imaging intervals, rates of sheath remodeling were normalized to a “% per week” unit by calculating the percent of remodeling sheaths, multiplied by 7, divided by the number of days between imaging sessions. The effect in length was analyzed analogously to the rate, by computing the total change in length generated by sheath remodeling (Figs. 2, F and I, and 4C and figs. S5C and S8B), relative to the total length of all myelin sheaths (Figs. 1K and 3, E and I, and fig. S4, E to G). When plotting total change in length by dynamics sheaths (Figs. 2I and 3, E and I, and fig. S5C) or changes in length due to elongations and contractions in the same plot (Figs. 1K and 4C), we reported absolute values for reduction in length. We analyzed the effect of MD on the cumulative change in myelin length (Fig. 3); for each individual animal, the change was considered an increase when the difference was >5% (MD versus before).

Confocal images to interrogate CPN myelination over time (fig. S3) were analyzed as described before for in vivo  $z$ -stacks.

### Analyzing integration of new myelinating oligodendrocytes

When we analyzed the integration of new myelinating oligodendrocytes (3), cells were

followed in three dimensions using custom FIJI scripts by defining eGFP<sup>+</sup> cell bodies at each time point and recording xyz coordinates. New eGFP<sup>+</sup> cells were identified as newly integrated myelinating oligodendrocytes when at least 20 new myelin sheaths were observed in close proximity (less than 60  $\mu\text{m}$ ) to the new oligodendrocyte soma (3). To report the density of oligodendrocytes (Fig. 3K), we normalized to the approximate average imaged volume (1.10<sup>-2</sup> mm<sup>3</sup>), such that the value represents the average number per imaging volume.

### Analyzing putative nodes of Ranvier

Putative nodes of Ranvier were identified by measuring the fluorescence intensity across the putative node; if the average intensity between adjacent myelin sheaths decreased below two times the shot noise background levels, and the length of the gap between eGFP<sup>+</sup> processes was <5  $\mu\text{m}$ , the structure was considered a node (3). Displacement of a node was defined as a shift >1.5  $\mu\text{m}$  of the node center to an area previously occupied by an eGFP<sup>+</sup> process.

### Analyzing axonal arbor

Axonal arbor remodeling was studied on PV-INs. Because of the high density of PV-IN processes in L2/3, we only examined the segments of axon that were myelinated at some point during the experiments and were confidently identifiable along their full length. Most of the combined axon and myelin remodeling events were observed when new myelin sheaths were produced on new axonal segments (Fig. 5E); however, it is possible that smaller contractions or elongations of axonal segments were undercounted due to stringency cutoffs for axonal tracing.

When plotting total change in axon length (fig. S10C), we considered absolute values for reduction in length to calculate the cumulative total change.

### Fluorescence immunohistochemistry

Immunohistochemistry was performed at P28 and onward time points in transgenic mice, as indicated in each figure. Animals were anesthetized with tribromoethanol (Avertin) and transcardially perfused with 0.1 M PBS (phosphate buffered saline; pH 7.4) followed by 4% paraformaldehyde, as described previously (39). Cortical tissue was then post-fixed overnight in 4% paraformaldehyde, followed by 3  $\times$  10 min washes in 0.1 M PBS. Serial coronal sections (40  $\mu\text{m}$  thick) were cut using a Leica microtome (VT1000 S), collected in PBS with 0.02% sodium azide and stored at 4°C. Free-floating sections were blocked for 1 hour at room temperature in blocking buffer [PBS with 0.02% sodium azide, 0.3% bovine serum albumin (BSA), 0.3% Triton X-100, and 8% serum of the species corresponding to the secondary antibody], and then incubated overnight

at 4°C in blocking buffer with the following primary antibodies: rat anti-MBP (monoclonal, 1:100, Millipore, MAB386, RRID:AB\_94975), rabbit anti-Parvalbumin (1:500, Swant, PV27; RRID:AB\_2631173), mouse anti-Rorβ (monoclonal, 1:100, Cosmo Bio, PPX-PP-N7927-00, RRID:AB\_1961850), rabbit anti-Cux1 (polyclonal, 1:100, Santa Cruz Biotechnology, sc-13024, RRID:AB\_2261231), mouse anti-Satb2 (monoclonal, 1:50, Abcam, ab51502, RRID:AB\_882455), rabbit anti-GABA (polyclonal, 1:1000, Sigma-Aldrich, A2052, RRID:AB\_477652), rabbit anti-Olig2 (1:100, IBL America, IBL 18953), rabbit anti-s100β (polyclonal, 1:2000, Abcam, ab41548, RRID:AB\_956280), mouse anti-Caspr (monoclonal, 1:100, UC Davis/NIH NeuroMab, 75-001, RRID:AB\_2083496), mouse anti-Pan-Nav1 (monoclonal, 1:100, UC Davis/NIH NeuroMab, 75-405, RRID:AB\_2491098), goat anti-PDGFRα (polyclonal, 1:200, Novus, AF1062, RRID:AB\_2236897), rabbit anti-Ki67 (polyclonal, 1:200, Abcam, ab15580, RRID:AB\_443209) and rabbit anti-cleaved-caspase-3 (polyclonal, 1:300, Cell Signaling, 9661, RRID:AB\_2341188). Secondary antibody (all 1:750, ThermoFisher) labeling was performed at room temperature for 2 hours as follows: goat anti-rat IgG (H+L) Alexa Fluor 647 (A-21247, RRID:AB\_141778), donkey anti-mouse immunoglobulin G (IgG) (H+L) Alexa Fluor 647 (A-31571, RRID:AB\_162542), goat anti-rabbit IgG (H+L) Alexa Fluor 488 (A-11008, RRID:AB\_143165), goat anti-mouse IgG (H+L) Alexa Fluor 647 (A-21236, RRID:AB\_141725), donkey anti-rabbit IgG (H+L) Alexa Fluor 546 (A10040, RRID:AB\_2534016) and donkey anti-goat IgG (H+L) Alexa Fluor 488 (A-11055, RRID:AB\_2534102). Sections were mounted using ProLong Gold (Invitrogen P36930). Confocal imaging was performed on a Zeiss LSM 700 microscope using three different lasers: FITC (488 nm laser line excitation; 522/35 emission filter), Cy3 (555 nm excitation; 583 emission), and Cy5 (639 nm excitation; 680/32 emission). The primary visual cortex was first identified using a 10x objective, and imaged using a 20x and 40x objectives with a z-step size of 0.99 μm and 0.47 μm, respectively.

#### Data presentation and statistical analysis

The statistical tests used to measure significance, the corresponding significance level (*P* value), and sample size are provided in table S1. Normality was assessed using Shapiro-Wilk's test at a *P* value of 0.05. When a data set did not satisfy normality criteria, nonparametric statistics were applied. Two-tailed Mann-Whitney *U* test was used for single comparisons, and two-tailed Wilcoxon matched-pairs signed rank test was used for paired values. For normal distributions, homoscedasticity was assessed using Bartlett's test and *F*-test, at a *P* value of 0.05. For homogeneous variances, two-tailed *t* test was used for single comparisons, repeated-

measures one-way analysis of variance (ANOVA) followed by post hoc Dunnett's test was used for statistical analysis of time course data, and two-way ANOVA was used for two-factor data sets. Paired *t* test was used to compare paired data. In the only case in which variances were not homogeneous, a *t* test with Welch's correction was used. Two-tailed Fisher's exact test (small sample size) or  $\chi^2$  test were used in the analysis of contingency tables. No statistical methods were used to predetermine sample sizes, but our sample sizes are similar to those reported in previous publications (2, 3, 17) and consistent with those used in the field. Unless otherwise specified, data are presented as mean ± SEM (text and figures); when the number of statistical independent replicates is greater than 15 per condition, individual values are not plotted for clarity (instead, we display a summary plot). When the data are displayed in a violin plot, we showed the median and the inter-quartile range (Fig. 1G). Statistical tests were performed using GraphPad Prism version 8.4.1 (GraphPad Software) or MATLAB 2018a (The MathWorks, Natick, MA), and *P* < 0.05 was considered statistically significant.

#### REFERENCES AND NOTES

- N. Baumann, D. Pham-Dinh, Biology of oligodendrocyte and myelin in the mammalian central nervous system. *Physiol. Rev.* **81**, 871–927 (2001). doi: [10.1152/physrev.2001.81.2.871](https://doi.org/10.1152/physrev.2001.81.2.871); pmid: [11274346](https://pubmed.ncbi.nlm.nih.gov/11274346/)
- R. A. Hill, A. M. Li, J. Grutzendler, Lifelong cortical myelin plasticity and age-related degeneration in the live mammalian brain. *Nat. Neurosci.* **21**, 683–695 (2018). doi: [10.1038/s41593-018-0120-6](https://doi.org/10.1038/s41593-018-0120-6); pmid: [29556031](https://pubmed.ncbi.nlm.nih.gov/29556031/)
- E. G. Hughes, J. L. Orthmann-Murphy, A. J. Langseth, D. E. Bergles, Myelin remodeling through experience-dependent oligodendrogenesis in the adult somatosensory cortex. *Nat. Neurosci.* **21**, 696–706 (2018). doi: [10.1038/s41593-018-0121-5](https://doi.org/10.1038/s41593-018-0121-5); pmid: [29556025](https://pubmed.ncbi.nlm.nih.gov/29556025/)
- E. M. Gibson *et al.*, Neuronal activity promotes oligodendrogenesis and adaptive myelination in the mammalian brain. *Science* **344**, 1252304 (2014). doi: [10.1126/science.1252304](https://doi.org/10.1126/science.1252304); pmid: [24727982](https://pubmed.ncbi.nlm.nih.gov/24727982/)
- R. D. Fields, A new mechanism of nervous system plasticity: Activity-dependent myelination. *Nat. Rev. Neurosci.* **16**, 756–767 (2015). doi: [10.1038/nrn4023](https://doi.org/10.1038/nrn4023); pmid: [26585800](https://pubmed.ncbi.nlm.nih.gov/26585800/)
- C. W. Mount, M. Monje, Wrapped to adapt: Experience-dependent myelination. *Neuron* **95**, 743–756 (2017). doi: [10.1016/j.neuron.2017.07.009](https://doi.org/10.1016/j.neuron.2017.07.009); pmid: [28817797](https://pubmed.ncbi.nlm.nih.gov/28817797/)
- S. Mensch *et al.*, Synaptic vesicle release regulates myelin sheath number of individual oligodendrocytes in vivo. *Nat. Neurosci.* **18**, 628–630 (2015). doi: [10.1038/nn.3991](https://doi.org/10.1038/nn.3991); pmid: [25849985](https://pubmed.ncbi.nlm.nih.gov/25849985/)
- I. A. McKenzie *et al.*, Motor skill learning requires active central myelination. *Science* **346**, 318–322 (2014). doi: [10.1126/science.1254960](https://doi.org/10.1126/science.1254960); pmid: [25324381](https://pubmed.ncbi.nlm.nih.gov/25324381/)
- A. C. Geraghty *et al.*, Loss of adaptive myelination contributes to methotrexate chemotherapy-related cognitive impairment. *Neuron* **103**, 250–265.e8 (2019). doi: [10.1016/j.neuron.2019.04.032](https://doi.org/10.1016/j.neuron.2019.04.032); pmid: [31122677](https://pubmed.ncbi.nlm.nih.gov/31122677/)
- S. Pan, S. R. Mayoral, H. S. Choi, J. R. Chan, M. A. Kheirbek, Preservation of a remote fear memory requires new myelin formation. *Nat. Neurosci.* **23**, 487–499 (2020). doi: [10.1038/s41593-019-0582-1](https://doi.org/10.1038/s41593-019-0582-1); pmid: [32042175](https://pubmed.ncbi.nlm.nih.gov/32042175/)
- M. Swire, Y. Kotelevtsev, D. J. Webb, D. A. Lyons, C. French-Constant, Endothelin signalling mediates experience-dependent myelination in the CNS. *eLife* **8**, e49493 (2019). doi: [10.7554/eLife.49493](https://doi.org/10.7554/eLife.49493); pmid: [31657718](https://pubmed.ncbi.nlm.nih.gov/31657718/)
- G. S. Tomassy *et al.*, Distinct profiles of myelin distribution along single axons of pyramidal neurons in the neocortex. *Science* **344**, 319–324 (2014). doi: [10.1126/science.1249766](https://doi.org/10.1126/science.1249766); pmid: [24744380](https://pubmed.ncbi.nlm.nih.gov/24744380/)
- K. D. Micheva *et al.*, A large fraction of neocortical myelin ensheathes axons of local inhibitory neurons. *eLife* **5**, e15784 (2016). doi: [10.7554/eLife.15784](https://doi.org/10.7554/eLife.15784); pmid: [27383052](https://pubmed.ncbi.nlm.nih.gov/27383052/)
- M. Zonouzi *et al.*, Individual oligodendrocytes show bias for inhibitory axons in the neocortex. *Cell Rep.* **27**, 2799–2808.e3 (2019). doi: [10.1016/j.celrep.2019.05.018](https://doi.org/10.1016/j.celrep.2019.05.018); pmid: [31167127](https://pubmed.ncbi.nlm.nih.gov/31167127/)
- D. H. Hubel, T. N. Wiesel, The period of susceptibility to the physiological effects of unilateral eye closure in kittens. *J. Physiol.* **206**, 419–436 (1970). doi: [10.1113/jphysiol.1970.sp009022](https://doi.org/10.1113/jphysiol.1970.sp009022); pmid: [5498493](https://pubmed.ncbi.nlm.nih.gov/5498493/)
- J. Stedehouder *et al.*, Fast-spiking parvalbumin interneurons are frequently myelinated in the cerebral cortex of mice and humans. *Cereb. Cortex* **27**, 5001–5013 (2017). doi: [10.1093/cercor/bhx203](https://doi.org/10.1093/cercor/bhx203); pmid: [28922832](https://pubmed.ncbi.nlm.nih.gov/28922832/)
- C. M. Bacmeister *et al.*, Motor learning promotes remyelination via new and surviving oligodendrocytes. *Nat. Neurosci.* **23**, 819–831 (2020). doi: [10.1038/s41593-020-0637-3](https://doi.org/10.1038/s41593-020-0637-3); pmid: [32424285](https://pubmed.ncbi.nlm.nih.gov/32424285/)
- F. Auer, S. Vagionitis, T. Czopka, Evidence for myelin sheath remodeling in the CNS revealed by in vivo imaging. *Curr. Biol.* **28**, 549–559.e3 (2018). doi: [10.1016/j.cub.2018.01.017](https://doi.org/10.1016/j.cub.2018.01.017); pmid: [29429620](https://pubmed.ncbi.nlm.nih.gov/29429620/)
- K. Kameyama *et al.*, Difference in binocularity and ocular dominance plasticity between GABAergic and excitatory cortical neurons. *J. Neurosci.* **30**, 1551–1559 (2010). doi: [10.1523/JNEUROSCI.5025-09.2010](https://doi.org/10.1523/JNEUROSCI.5025-09.2010); pmid: [20107082](https://pubmed.ncbi.nlm.nih.gov/20107082/)
- J. L. Chen *et al.*, Structural basis for the role of inhibition in facilitating adult brain plasticity. *Nat. Neurosci.* **14**, 587–594 (2011). doi: [10.1038/nn.2799](https://doi.org/10.1038/nn.2799); pmid: [21478885](https://pubmed.ncbi.nlm.nih.gov/21478885/)
- J. L. Chen *et al.*, Clustered dynamics of inhibitory synapses and dendritic spines in the adult neocortex. *Neuron* **74**, 361–373 (2012). doi: [10.1016/j.neuron.2012.02.030](https://doi.org/10.1016/j.neuron.2012.02.030); pmid: [22542188](https://pubmed.ncbi.nlm.nih.gov/22542188/)
- M. C. Ford *et al.*, Tuning of Ranvier node and internode properties in myelinated axons to adjust action potential timing. *Nat. Commun.* **6**, 8073 (2015). doi: [10.1038/ncomms9073](https://doi.org/10.1038/ncomms9073); pmid: [26305015](https://pubmed.ncbi.nlm.nih.gov/26305015/)
- T. Tagoe, M. Barker, A. Jones, N. Allcock, M. Hamann, Auditory nerve periodical dysmyelination in noise-induced hearing loss. *J. Neurosci.* **34**, 2684–2688 (2014). doi: [10.1523/JNEUROSCI.3977-13.2014](https://doi.org/10.1523/JNEUROSCI.3977-13.2014); pmid: [24523557](https://pubmed.ncbi.nlm.nih.gov/24523557/)
- S. A. Marik, H. Yamahachi, S. Meyer zum Alten Borgloh, C. D. Gilbert, Large-scale axonal reorganization of inhibitory neurons following retinal lesions. *J. Neurosci.* **34**, 1625–1632 (2014). doi: [10.1523/JNEUROSCI.4345-13.2014](https://doi.org/10.1523/JNEUROSCI.4345-13.2014); pmid: [24478346](https://pubmed.ncbi.nlm.nih.gov/24478346/)
- H. Wake, P. R. Lee, R. D. Fields, Control of local protein synthesis and initial events in myelination by action potentials. *Science* **333**, 1647–1651 (2011). doi: [10.1126/science.1206998](https://doi.org/10.1126/science.1206998); pmid: [21817014](https://pubmed.ncbi.nlm.nih.gov/21817014/)
- M. Makinodan, K. M. Rosen, S. Ito, G. Corfas, A critical period for social experience-dependent oligodendrocyte maturation and myelination. *Science* **337**, 1357–1360 (2012). doi: [10.1126/science.1220845](https://doi.org/10.1126/science.1220845); pmid: [22984073](https://pubmed.ncbi.nlm.nih.gov/22984073/)
- K. B. Hengen, M. E. Lambo, S. D. Van Hooser, D. B. Katz, G. G. Turrigiano, Firing rate homeostasis in visual cortex of freely behaving rodents. *Neuron* **80**, 335–342 (2013). doi: [10.1016/j.neuron.2013.08.038](https://doi.org/10.1016/j.neuron.2013.08.038); pmid: [24139038](https://pubmed.ncbi.nlm.nih.gov/24139038/)
- B. M. Hooks, C. Chen, Circuitry underlying experience-dependent plasticity in the mouse visual system. *Neuron* **106**, 21–36 (2020). doi: [10.1016/j.neuron.2020.01.031](https://doi.org/10.1016/j.neuron.2020.01.031); pmid: [32272065](https://pubmed.ncbi.nlm.nih.gov/32272065/)
- K. P. Berry, E. Nedivi, Experience-dependent structural plasticity in the visual system. *Annu. Rev. Vis. Sci.* **2**, 17–35 (2016). doi: [10.1146/annurev-vision-111815-114638](https://doi.org/10.1146/annurev-vision-111815-114638); pmid: [28532358](https://pubmed.ncbi.nlm.nih.gov/28532358/)
- A. H. Seidl, Regulation of conduction time along axons. *Neuroscience* **276**, 126–134 (2014). doi: [10.1016/j.neuroscience.2013.06.047](https://doi.org/10.1016/j.neuroscience.2013.06.047); pmid: [23820043](https://pubmed.ncbi.nlm.nih.gov/23820043/)
- M. Salami, C. Itami, T. Tsumoto, F. Kimura, Change of conduction velocity by regional myelination yields constant latency irrespective of distance between thalamus and cortex. *Proc. Natl. Acad. Sci. U.S.A.* **100**, 6174–6179 (2003). doi: [10.1073/pnas.0937380100](https://doi.org/10.1073/pnas.0937380100); pmid: [12719546](https://pubmed.ncbi.nlm.nih.gov/12719546/)
- B. S. Mallon, H. E. Shick, G. J. Kidd, W. B. Macklin, Proteolipid promoter activity distinguishes two populations of NG2-positive cells throughout neonatal cortical development. *J. Neurosci.* **22**, 876–885 (2002). doi: [10.1523/JNEUROSCI.22-03-00876.2002](https://doi.org/10.1523/JNEUROSCI.22-03-00876.2002); pmid: [11826117](https://pubmed.ncbi.nlm.nih.gov/11826117/)

33. S. Hippenmeyer *et al.*, A developmental switch in the response of DRG neurons to ETS transcription factor signaling. *PLoS Biol.* **3**, e159 (2005). doi: [10.1371/journal.pbio.0030159](https://doi.org/10.1371/journal.pbio.0030159); pmid: [15836427](https://pubmed.ncbi.nlm.nih.gov/15836427/)
34. K. S. Matho *et al.*, Genetic dissection of glutamatergic neuron subpopulations and developmental trajectories in the cerebral cortex. *bioRxiv* 054064 [Preprint] 24 April 2020. <https://doi.org/10.1101/2020.04.22.054064>.
35. L. Madisen *et al.*, A robust and high-throughput Cre reporting and characterization system for the whole mouse brain. *Nat. Neurosci.* **13**, 133–140 (2010). doi: [10.1038/nn.2467](https://doi.org/10.1038/nn.2467); pmid: [20023653](https://pubmed.ncbi.nlm.nih.gov/20023653/)
36. W. C. A. Lee *et al.*, Dynamic remodeling of dendritic arbors in GABAergic interneurons of adult visual cortex. *PLoS Biol.* **4**, e29 (2006). doi: [10.1371/journal.pbio.0040126](https://doi.org/10.1371/journal.pbio.0040126); pmid: [16366735](https://pubmed.ncbi.nlm.nih.gov/16366735/)
37. K. L. Villa *et al.*, Inhibitory synapses are repeatedly assembled and removed at persistent sites in vivo. *Neuron* **89**, 756–769 (2016). doi: [10.1016/j.neuron.2016.01.010](https://doi.org/10.1016/j.neuron.2016.01.010); pmid: [26853302](https://pubmed.ncbi.nlm.nih.gov/26853302/)
38. M. Sato, M. P. Stryker, Distinctive features of adult ocular dominance plasticity. *J. Neurosci.* **28**, 10278–10286 (2008). doi: [10.1523/JNEUROSCI.2451-08.2008](https://doi.org/10.1523/JNEUROSCI.2451-08.2008); pmid: [18842887](https://pubmed.ncbi.nlm.nih.gov/18842887/)
39. P. Arlotta *et al.*, Neuronal subtype-specific genes that control corticospinal motor neuron development in vivo. *Neuron* **45**, 207–221 (2005). doi: [10.1016/j.neuron.2004.12.036](https://doi.org/10.1016/j.neuron.2004.12.036); pmid: [15664173](https://pubmed.ncbi.nlm.nih.gov/15664173/)

#### ACKNOWLEDGMENTS

We thank J. R. Brown, P. Oyler-Castrillo, and former and present members of the Arlotta and Nedivi laboratories for insightful discussions and editing of the manuscript; J. Huang and W. Macklin for sharing the Tbr2<sup>CreERT2</sup> and the Plp1-eGFP mouse lines, respectively; J. Boivin for helpful advice on in vivo 2P-imaging; V. Vuong for outstanding technical support and for help with image analysis; and B. Paulsen for help with figure production. **Funding:** This work was supported by grants from the Stanley Center for Psychiatric Research, the Broad Institute of MIT and Harvard, the National Institute of Mental Health (U19MH114821 and P50MH094271 to P.A.), the National Institutes of Health (RO1-EY025437 to E.N.), and the JBP Foundation to E.N.; K.M. acknowledges support by the DFG fellowship (MI 2108/1-1). **Author contributions:** P.A., E.N., and S.M.Y. conceived the experiments. S.M.Y. performed all the

experiments, with help from K.M.; S.M.Y. analyzed data, with help from V.J.; and P.A., E.N., and S.M.Y. wrote the manuscript with contributions from all authors. All authors read and approved the final manuscript. **Competing interests:** The authors declare no competing interests. **Data and materials availability:** All data are available in the main text or the supplementary materials. Request for materials should be addressed to P.A. ([paola\\_arlotta@harvard.edu](mailto:paola_arlotta@harvard.edu)) and S.M.Y. ([sungminyang@fas.harvard.edu](mailto:sungminyang@fas.harvard.edu)).

#### SUPPLEMENTARY MATERIALS

[science.sciencemag.org/content/370/6523/eabd2109/suppl/DC1](https://science.sciencemag.org/content/370/6523/eabd2109/suppl/DC1)  
Figs. S1 to S10  
Table S1  
Movies S1 to S3  
MDAR Reproducibility Checklist  
[View/request a protocol for this paper from Bio-protocol.](#)

8 June 2020; accepted 26 October 2020  
10.1126/science.abd2109

## Neuron class–specific responses govern adaptive myelin remodeling in the neocortex

Sung Min Yang, Katrin Michel, Vahbiz Jokhi, Elly Nedivi and Paola Arlotta

*Science* **370** (6523), eabd2109.  
DOI: 10.1126/science.abd2109

### Cellular effects of visual deprivation

Myelination speeds the progress of action potentials along neuronal axons. Yang *et al.* studied changes in myelination in the mouse visual cortex in response to visual experience (see the Perspective by Yalçın and Monje). With normal vision, myelination is continuously remodeled. As ocular dominance shifts in response to monocular deprivation, myelination patterns change on certain inhibitory interneurons but not on excitatory callosal projection neurons. Myelin sheaths are both added and subtracted, segments of myelin elongate and contract, and preexisting oligodendrocytes make new myelin sheaths. This adaptive myelination helps to diversify neuronal function and remodel neuronal circuits in response to sensory experience.

*Science*, this issue p. eabd2109; see also p. 1414

#### ARTICLE TOOLS

<http://science.sciencemag.org/content/370/6523/eabd2109>

#### SUPPLEMENTARY MATERIALS

<http://science.sciencemag.org/content/suppl/2020/12/16/370.6523.eabd2109.DC1>

#### RELATED CONTENT

<http://science.sciencemag.org/content/sci/370/6523/1414.full>

#### REFERENCES

This article cites 39 articles, 12 of which you can access for free  
<http://science.sciencemag.org/content/370/6523/eabd2109#BIBL>

#### PERMISSIONS

<http://www.sciencemag.org/help/reprints-and-permissions>

Use of this article is subject to the [Terms of Service](#)

---

*Science* (print ISSN 0036-8075; online ISSN 1095-9203) is published by the American Association for the Advancement of Science, 1200 New York Avenue NW, Washington, DC 20005. The title *Science* is a registered trademark of AAAS.

Copyright © 2020 The Authors, some rights reserved; exclusive licensee American Association for the Advancement of Science. No claim to original U.S. Government Works